Interaction effects of pseudospin-based magnetic monopoles and kinks in a doped dipolar superlattice gas

Xiang Gao,[1] Shao-Jun Li,[1] Shou-Long Chen,[1] Xue-Ting Fang,[1] Qian-Ru Zhu,[1] Xing Deng,[1] Lushuai Cao,[1,*] Peter Schmelcher,[2,3] and Zhong-Kun Hu[1,†]

[1]*MOE Key Laboratory of Fundamental Physical Quantities Measurement and Hubei Key Laboratory of Gravitation and Quantum Physics, PGMF and School of Physics, Huazhong University of Science and Technology, Wuhan 430074, China*

[2]*Zentrum für optische Quantentechnologien, Universität Hamburg, Luruper Chaussee 149, 22761 Hamburg, Germany*

[3]*The Hamburg Centre for Ultrafast Imaging, Universität Hamburg, Luruper Chaussee 149, 22761 Hamburg, Germany*

(Received 30 November 2021; revised 10 April 2022; accepted 11 April 2022; published 20 May 2022)

Magnetic monopoles and kinks are topological excitations that have been extensively investigated in quantum spin systems, but usually, they are studied in different setups. We explore the conditions for the coexistence and interaction effects of these quasiparticles in the pseudospin chain of an atomic dipolar superlattice gas. In this chain, the magnetic kink is the intrinsic quasiparticle, and the particle (hole) defect takes over the role of the north (south) magnetic monopole, exerting monopolar magnetic fields on neighboring spins. A binding effect between the monopole and kink is revealed, which renormalizes the dispersion of the kink. The corresponding dynamical antibinding process is observed and arises due to the kink-antikink annihilation. The rich interaction effects of the two quasiparticles could stimulate corresponding investigations in bulk spin systems.

DOI: 10.1103/PhysRevA.105.053308

I. INTRODUCTION

Quantum spin systems possess various topological excitations, such as magnetic kinks [1,2], spinons [3,4], skyrmions [5], Majorana modes [6], and magnetic monopoles [7–10]. These quasiparticles possess rich magnetic properties and endow spin systems with potential applications, such as functional spintronic devices [11–13]. The interaction between different quasiparticles is of particular importance since it not only enriches the dynamical properties of spin systems but also provides efficient manipulation tools for corresponding applications. The coexistence and interaction effects between different quasiparticles, such as a magnon and a spinon [14,15], a kink and a magnon [16], and a magnon and a skyrmion [17–19], have been extensively investigated. Appealing coupling effects have been revealed between these quasiparticles, which has led to the demand for an investigation of so far unknown interaction effects of magnetic quasiparticles, specifically the monopole and the kink. This could be explored both in condensed-matter spin systems and in pseudospin systems emulated with, e.g., ultracold atomic gases.

Ultracold atomic gases have become one of the major platforms for quantum simulation [20–40] thanks to the rich degrees of freedom of the atomic gas to construct the target Hilbert space and the tunability to engineer the demanded Hamiltonians. Concerning quantum simulation of spin systems, the target spin degree of freedom can be modeled by the atomic species [21,22], the atomic internal states [23–30], and the spatial modes of the lattice atoms, such as the occupation states in tilted lattices [31] or superlattices [32–35]. Effective interactions such as spin-spin interactions [26] and spin-orbital couplings [32,33] have also been engineered. Various magnetic quasiparticles have been simulated, such as magnons [23], spinons [24], magnetic polarons [27,28], and magnetic kinks [29,30,34]. Particularly, magnetic monopoles of different types have been both theoretically and experimentally implemented for atomic Bose-Einstein condensates [36–40], with the generation, dynamical properties, and interaction effects investigated.

The magnetic monopoles generated in ultracold atomic [36–40] and condensed-matter systems [7–10] are mainly embedded in the superfluid and spin-ice phases, respectively, in which the excitation condition and dynamical properties of the monopoles have been extensively investigated. These magnetic phases, however, can hardly sustain the coexistence of the monopole with other magnetic quasiparticles and hinder the investigation of their coupling effects. In this paper we propose a quantum simulation scheme which generates the monopole on the ferromagnetic host background and enables the coexistence of and interaction between the monopole and the intrinsic ferromagnetic quasiparticle, i.e., the kink. Our simulation scheme adapts and generalizes the pseudospin mapping of ultracold atoms in a double-well superlattice, which has been exploited to simulate spin-orbit coupling [32] and the corresponding supersolidlike phase [33], as well as magnetic phase transitions [34] and quasiparticles [35]. Based on this simulation scheme, we show that the monopole can exert an attractive interaction with the kink through the monopolar magnetic field, which gives rise to the binding of the two quasiparticles. The binding can also be released by a kink-antikink annihilation. In essence, our simulation

*lushuaïcao@hust.edu.cn
†zkhu@hust.edu.cn

scheme comprises coupling effects of the magnetic monopole to other magnetic quasiparticles and reveals their binding and antibinding transition. It provides a tool to control and manipulate the dynamics of magnetic monopoles.

This paper is organized as follows. In Sec. II, we demonstrate the pseudospin chain based on the dipolar superlattice gas. In Sec. III, we focus on the interaction effects between the north monopole and kink. A brief discussion and outlook are given in Sec. IV.

II. SETUP AND PSEUDOSPIN MAPPING

We consider the dipolar superlattice gas (DSG) of spin-polarized fermions confined in the one-dimensional double-well superlattice, in which the fermions interact with each other through the repulsive dipole-dipole interaction (DDI) [41]. The DSG system can be described by the following Fermi-Hubbard Hamiltonian:

$$\hat{H}_{\rm FH} = -J\sum_{i=1}^{M}(\hat{f}_{2i}^{\dagger}\hat{f}_{2i-1} + \text{H.c.}) - J_1\sum_{i=1}^{M-1}(\hat{f}_{2i}^{\dagger}\hat{f}_{2i+1} + \text{H.c.}) + \sum_{i<j\in[1,2M]} V_d(j-i)\hat{n}_i\hat{n}_j, \tag{1}$$

where $\hat{f}_{2i-1/2i}^{\dagger}$ and $\hat{f}_{2i-1/2i}$ are the fermionic creation and annihilation operators on the left (right) site of the ith supercell and the operator $\hat{n}_i = \hat{f}_i^{\dagger}\hat{f}_i$ counts the number of fermions at site i. The first two terms in $\hat{H}_{\rm FH}$ describe the intra- and intercell hopping, respectively, with hopping amplitudes $J \gg J_1$. The DDI between two fermions located in the ith and jth sites is taken to be $V_d(j-i) = d/|x_j - x_i|^3$, where x_i (x_j) is the local minimum of the corresponding site, and d denotes the DDI strength. Without loss of generality, we take $J = 10J_1$ and $(x_{2j} - x_{2j-1})/(x_{2j+1} - x_{2j}) = 1/2$, with the lattice constant $a = x_{2j+1} - x_{2j-1}$. We further truncate the DDI to the nearest-neighbor interaction, which presents a good approximation for the parameter regime explored in this paper.

The pseudospin mapping transfers the DSG system to an effective spin chain, and we generalize it and bring in defects to the spin chain. Under the tight-binding approximation, each cell of the DSG system accommodates four local occupation states of $\{|1,0\rangle_i, |0,1\rangle_i, |1,1\rangle_i, |0,0\rangle_i\}$, where $|n_L, n_R\rangle_i$ denotes n_L and n_R fermions occupying the left and right sites of the ith cell, respectively. In the pseudospin mapping, the single-occupation states $|1,0\rangle_i$ and $|0,1\rangle_i$ are mapped to the spin states $|\leftarrow\rangle_i$ and $|\rightarrow\rangle_i$ at the ith site of the chain. We further map the double occupation $|1,1\rangle_i$ and local vacuum state $|0,0\rangle_i$ to the particle and hole defects of the spin chain, denoted by $|P\rangle_i$ and $|H\rangle_i$, respectively. Under the pseudospin mapping, the DSG system is mapped to an effective spin chain, with the Hamiltonian $\hat{H}_{\rm spin}^{\rm DSG} = \hat{H}_0 + \hat{H}_{\rm SD}$:

$$\hat{H}_0 = -J\sum_{\alpha=1}^{M}\hat{\sigma}_x^{\alpha} - \frac{d}{4}\sum_{\alpha=1}^{M-1}\hat{\sigma}_z^{\alpha}\hat{\sigma}_z^{\alpha+1} + \frac{d}{2}\sum_{\alpha=1}^{M}\tilde{\sigma}_z^{\alpha} + \frac{d}{4}\left(\hat{\sigma}_z^{1} - \hat{\sigma}_z^{M}\right) + \frac{d}{4}\left(\tilde{\sigma}_z^{1} + \tilde{\sigma}_z^{M}\right), \tag{2}$$

$$\hat{H}_{\rm SD} = \frac{d}{4}\sum_{\alpha=1}^{M}\tilde{\sigma}_z^{\alpha}\left(\hat{\sigma}_z^{\alpha-1} - \hat{\sigma}_z^{\alpha+1}\right) - J_1\sum_{\alpha=1}^{M-1}\left[\left(\hat{s}_{\rightarrow,H}^{\alpha}\hat{s}_{H,\leftarrow}^{\alpha+1} + \text{H.c.}\right) + \left(\hat{s}_{\leftarrow,P}^{\alpha}\hat{s}_{P,\rightarrow}^{\alpha+1} + \text{H.c.}\right)\right] - J_1\sum_{\alpha=1}^{M-1}\left[\left(\hat{s}_{H,\rightarrow}^{\alpha}\hat{s}_{P,\rightarrow}^{\alpha+1} + \text{H.c.}\right) + \left(\hat{s}_{P,\leftarrow}^{\alpha}\hat{s}_{H,\leftarrow}^{\alpha+1} + \text{H.c.}\right)\right]. \tag{3}$$

In $\hat{H}_0$, $\hat{\sigma}_x^{\alpha}$ and $\hat{\sigma}_z^{\alpha}$ are the Pauli operators exerted on the pseudospins, and $\tilde{\sigma}_z^{\alpha} \equiv |P\rangle_\alpha\langle P| - |H\rangle_\alpha\langle H|$ is the effective Pauli operator exerted on the defects. To describe the counterpropagation of the defect and pseudospin, the exchange operator is introduced in $\hat{H}_{\rm SD}$, defined as $\hat{s}_{\Lambda,\sigma}^{\alpha} \equiv |\Lambda\rangle_\alpha\langle\sigma|$, with $\Lambda \in \{P, H\}$ and $\sigma \in \{\rightarrow, \leftarrow\}$. In the following, we call the effective spin chain the DSG pseudospin chain.

The DSG pseudospin chain is manifested as a transverse Ising spin chain, whose pseudospins interact by the Ising-type spin-spin interaction and are subjected to a transverse magnetic field, as indicated by the first two terms in $\hat{H}_0$. The fourth term in $\hat{H}_0$ refers to the antiparallel boundary magnetic (ABM) field localized at the two edges of the chain. The ABM field has been recognized as an efficient way to excite a kink since the original studies on magnetic kinks [1,42–44], and it gives rises to an intrinsic kink in the DSG pseudospin chain. More interestingly, as indicated by the last term in $\hat{H}_0$, the ABM fields also exert an attractive (repelling) potential to the hole (particle) defect along the direction of the field, which mimics the response of the magnetic south (north) monopole to the external magnetic field.

Besides the response to the magnetic field, further fingerprints of the magnetic monopole, i.e., the monopolar magnetic field and the Dirac string, are also reproduced by the particle and hole defects, which causes the particle and hole defects to well resemble the north monopole (NM) and south monopole (SM), respectively. The monopolar magnetic field is normally evidenced by the spin texture around the monopole, and as indicated by the first term in $\hat{H}_{\rm SD}$, the particle (hole) defect polarizes the neighbor spins away from (towards) the defect, which resembles the monopolar magnetic field surrounding the NM (SM). The second term in $\hat{H}_{\rm SD}$ further demonstrates that the hopping of the defects is accompanied by the flipping of the counterpropagating spin, which has been recognized as a signature of the Dirac string for the monopoles [7–10]. The last term in $\hat{H}_{\rm SD}$ refers to the pair production of a NM and a SM, which manifests as the main excitation channel of the monopoles in spin ices.

The DSG pseudospin chain is sketched in Fig. 1(a), where the ABM and the monopolar magnetic field around the NM and SM are schematically shown. Figure 1(b) shows the expectation values of $\langle\hat{\sigma}_z\rangle$ and $\langle\hat{\sigma}_x\rangle$ of the pseudospins around a localized NM in the paramagnetic phase, in which the transverse magnetic field aligns the pseudospins in the x direction. It can be seen that the pseudospins far away from the NM align along the transverse direction, while the spins neighboring the NM are polarized away from the NM, as indicated by the spin texture at the bottom of Fig. 1(b). Figure 1(c) summarizes the pair production and spin-flipping effects of $\hat{H}_{\rm SD}$ with a dynamical process in which, initially, a pair of monopoles is excited and then they hop away from each other, accompanied by the spin flipping. A detailed sketch of the pseudospin

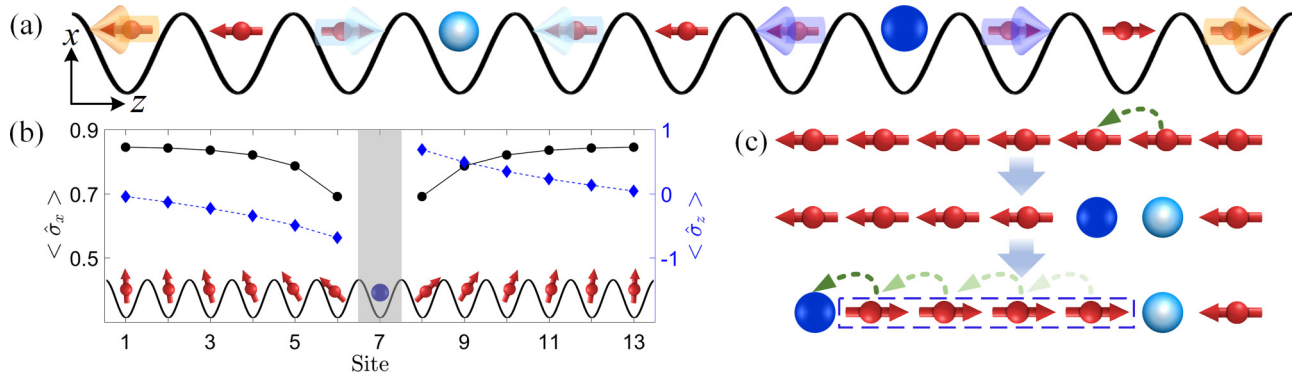

FIG. 1. (a) The pseudospin chain based on the DSG system. The NM and SM are sketched with the dark and light blue balls, respectively. The transparent orange and dark and light blue arrows refer to the ABM and the monopolar magnetic fields around the NM and SM, respectively. (b) The polarization of neighboring spins around a localized NM, in terms of $\langle\hat{\sigma}_x\rangle$ (solid lines) and $\langle\hat{\sigma}_z\rangle$ (dashed lines). The spin polarization is also explicitly shown at the bottom. (c) The dynamical process of the pair excitation, the tunneling of the NM and SM, and the spin flipping along the tunneling are shown.

mapping and a comparison of the spin polarization around the NM, SM, and a normal magnetic defect in the pseudospin chain are given in Appendixes A and B, respectively.

III. INTERACTION EFFECTS BETWEEN THE NM AND KINK

In the strong-interaction regime, the DSG pseudospin chain sustains the coexistence of the magnetic monopole and kinks and provides an ideal platform to investigate the interplay of the two quasiparticles. Here, we focus on the doping of a single NM defect to the DSG chain, and the results can be straightforwardly generalized to the SM doping. We define the tail-to-tail and head-to-head kinks as the kink and antikink, respectively. The Hilbert space is truncated to the subspace spanned by the basis states $|n\rangle_{\rm NM}\otimes|\tilde{\alpha}_0,\tilde{\alpha}_1\cdots\tilde{\alpha}_{2N}\rangle$, in which $|n\rangle_{\rm NM}$ denotes the position of the monopole and $|\tilde{\alpha}_0,\tilde{\alpha}_1\cdots\tilde{\alpha}_{2N}\rangle = |\cdots\leftarrow\leftarrow_{\tilde{\alpha}_0-1}\rightarrow\cdots\rightarrow_{\tilde{\alpha}_1-1}\leftarrow\cdots\leftarrow_{\tilde{\alpha}_{2N}-1}\rightarrow\cdots\rangle$ indicates the location of the (anti)kinks in the squeezed space where the monopole site is removed [24,45] (more details of the definition of the squeezed space are given in Appendix C). Accordingly, the Hamiltonian can be spanned in the monopole-kink subspace as $\hat{H}_{\rm doped-spin}=\hat{H}_{\rm K}+\hat{H}_{\rm NM-K}$, in which,

$$\hat{H}_{\rm K}=d\sum_{\tilde{\alpha}=1}^{M}\hat{n}_A^{\tilde{\alpha}}-J\sum_{\tilde{\alpha}=1}^{M-1}(\hat{S}_+^{\tilde{\alpha}}+\hat{S}_-^{\tilde{\alpha}})(\hat{S}_+^{\tilde{\alpha}+1}+\hat{S}_-^{\tilde{\alpha}+1}),\quad(4)$$

$$\hat{H}_{\rm NM-K}=-d\sum_{\alpha=\tilde{\alpha}}^{M}\hat{n}_K^{\tilde{\alpha}}\hat{n}_N^{\alpha}-J_1\sum_{\alpha=\tilde{\alpha}}^{M-1}\left(\hat{b}_N^{\alpha\,\dagger}\hat{b}_N^{\alpha+1}\hat{S}_-^{\tilde{\alpha}}\hat{S}_+^{\tilde{\alpha}+1}+\text{H.c.}\right).\quad(5)$$

In $\hat{H}_{\rm K}$, $\hat{n}_A^{\tilde{\alpha}}$ refers to the number of antikinks between sites $\tilde{\alpha}$ and $\tilde{\alpha}+1$ in the squeezed space, and $\hat{S}_{+/-}^{\tilde{\alpha}\dagger}=(\hat{a}_A^{\tilde{\alpha}\dagger}+\hat{a}_K^{\tilde{\alpha})}/(\hat{a}_A^{\tilde{\alpha}}+\hat{a}_K^{\tilde{\alpha}\dagger})$ combines the creation of a kink and the annihilation of an antikink. In $\hat{H}_{\rm NM-K}$, $\hat{b}_N^{\alpha\dagger}$ ($\hat{b}_N^{\alpha}$) denotes the creation (annihilation) of a NM on the αth site, with $\hat{n}_N^{\alpha}=\hat{b}_N^{\alpha\dagger}\hat{b}_N^{\alpha}$. $\hat{H}_{\rm NM-K}$ then describes the interaction between the monopole and kinks, which includes the attractive interaction between a NM and a kink and the effect of monopole hopping on the (anti)kink.

The effects of interaction between the NM and the (anti)kinks can be captured by the dynamical structure factor $S(k,\omega)$ [46,47], and $S(k,\omega)$ of the DSG pseudospin chain is shown in Fig. 2(a) and is calculated using the multilayer, multiconfiguration, time-dependent Hartree method for arbitrary bosonic (fermionic) mixtures [48–50] (for more details see Appendix D). In Fig. 2(a), a single-mode branch appears in the first band and gives a strong hint that the doped NM and the intrinsic kink are bound and behave as a single composite quasiparticle. The emergence of the NM-kink bound state can be confirmed by the NM-kink correlation $\langle\psi|\hat{n}_K^{\tilde{\alpha}}\hat{n}_N^{\beta}|\psi\rangle$, with $|\psi\rangle$ running through all eigenstates in the first band. Figure 2(b) shows the NM-kink correlation for an arbitrary eigenstate in the first band, and it clearly demonstrates that the NM and the intrinsic kink always occupy the same site. The NM-kink correlations for the other eigenstates in the first band all present the same bound behavior (not shown here).

The second band in Fig. 2(a) presents a broad spectrum, leading to a continuum band in the infinitely long chain limit. It is known that in the absence of the NM, the antikink-kink pair excitation dominates the excitation from the ground to higher bands, which leads to continuum excited bands in the infinite-chain limit. An analysis using the multiparticle correlations, however, reveals that the presence of a NM not only preserves the excitation channel of the antikink-kink pair excitation but also brings in a new channel contributing to the second band, which is the deconfinement of the NM and the intrinsic kink. Multiparticle correlations have become powerful and experimentally accessible tools to identify quasiparticle excitation in ultracold-atom simulated pseudospin chains [51], and here, we determine the four-body correlation $C_4=\sum_{\alpha,\beta,\gamma}\langle\hat{n}_K^{\alpha}\hat{n}_N^{\alpha}\hat{n}_K^{\beta}\hat{n}_A^{\gamma}\rangle$ and the three-body correlation $C_3=\sum_{\alpha,\beta}\langle(1-\hat{n}_K^{\alpha})\hat{n}_N^{\alpha}\hat{n}_K^{\beta}\rangle$ to identify the excitation channels from the first to the second band, where α, β, and γ run over all sites in the (squeezed) chain with $\alpha\neq\beta$. C_4 and C_3 signify the antikink-kink pair excitation in the presence of the bound NM-kink and the deconfinement of the bound NM-kink, respectively. The nonvanishing correlations

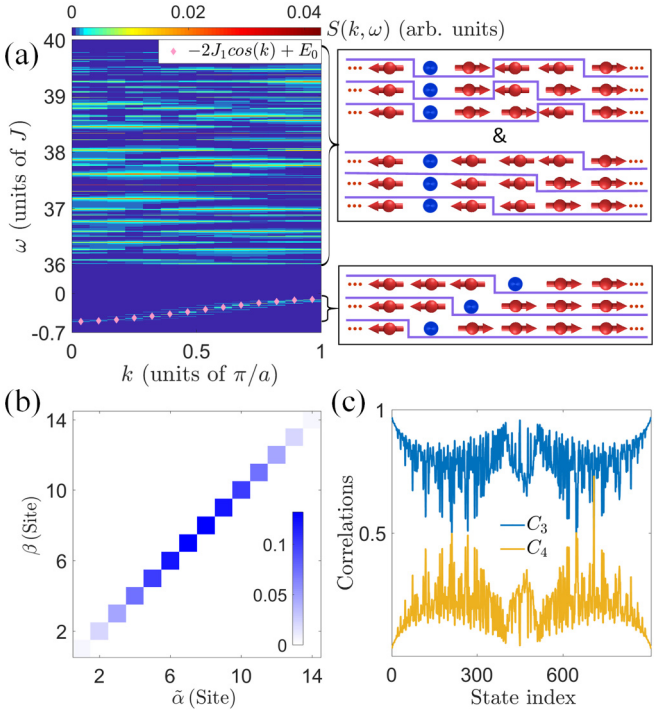

FIG. 2. (a) The dynamical structure factor $S(k,\omega)$ for the 14-site pseudospin chain with $d = 40J$. The frequency interval of $\omega \in (0.5, 36)$ is removed where the gap between the first two bands lies. The representative basis states contributed to each band are shown to the right of the structure factor plot, where different ferromagnetic domains are emphasized with solid-line steps and the (anti)kinks locate at the edges of the steps. The pink diamonds in the main plot are the band dispersion obtained from the effective single-particle Hamiltonian describing the emergent particle composed of the monopole and kink. (b) The NM-kink correlation for the ground state. (c) The three-body correlation C_3 (blue) and four-body correlation C_4 (yellow) of the second band.

C_4 and C_3 for the eigenstates in the second band, shown in Fig. 2(c), demonstrate that both excitation channels contribute to the second band and also suggest that the excitation of an antikink-kink pair can be transformed to the deconfinement state of the NM-kink bond, which has potential applications for the manipulation of monopoles and kinks. In Fig. 2, the boxes to the right of Fig. 2(a) sketch the dominant contributions to the first two bands, and from bottom to top they are the NM-kink bound state, the free pair of a NM and a kink, and the coexistence of the bound NM-kink with the antikink-kink pair.

It is well known that composite quasiparticles composed of two types of particles, such as polarons [52,53], can renormalize the dispersion and mobility of the bare particles and provide a unique control tool. The NM-kink bound state also shares this renormalization effect with the bare kink. As shown in Fig. 3, the dispersion of the bound state is significantly changed from that of the bare kink and can be tuned by the mobility of the NM. Furthermore, to verify the manipulation of the bound NM-kink by the antikink-kink pair excitation, we determine the dynamical process with the initial state where a bound NM-kink and an antikink-kink pair are

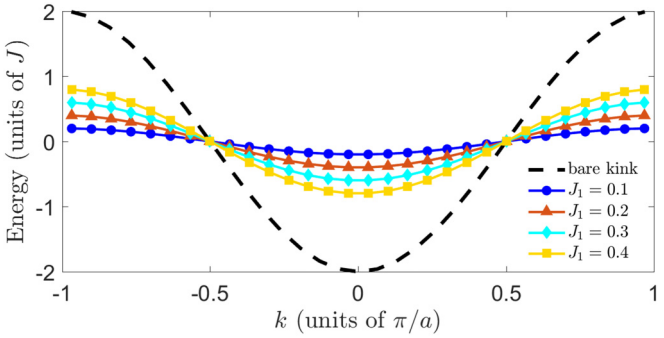

FIG. 3. The dispersions of a bare kink (black dashed line) and the composite quasiparticle for $J_1 = 0.1$ (blue circles), 0.2 (brown triangles), 0.3 (cyan diamonds), and 0.4 (yellow squares).

located at the left and right edges of the pseudospin chain. The temporal evolutions of $C_3(t)$ and $C_4(t)$ as shown in Fig. 4(a) indicate that, at the beginning of the dynamics, the system is dominated by the coexistence of the bound NM-kink and the antikink-kink pairs, whereas for later times (marked by gray vertical lines), the deconfinement of the bound NM-kink takes place, accompanied by the disappearance of the coexistence of the NM-kink and antikink-kink pairs. This confirms that the antikink-kink pair excitation can induce the deconfinement through the annihilation of the antikink with the kink bound to the NM.

In Figs. 4(b)–4(d), we also show the spatial densities of the NM, kink, and antikink at the beginning and later times marked in Fig. 4(a). The densities clearly show that in the beginning the NM-kink and antikink-kink pairs are separately located on opposite edges, and at later times the NM and kink become deconfined, with the antikink almost vanishing. The spatial densities further verify the deconfinement of the bound NM-kink by the antikink-kink annihilation process. The renormalization effect and the manipulation of the NM-kink bound state with the antikink suggest rich interaction effects between the NM and the (anti)kinks and provide a potential control of the kink by monopoles.

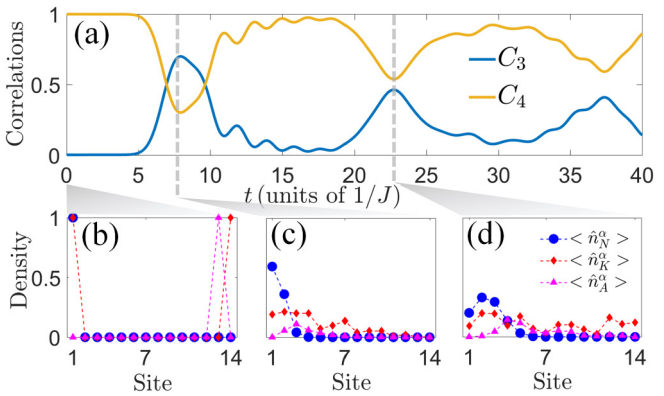

FIG. 4. (a) Temporal evolution of C_3 (blue) and C_4 (yellow) during the dynamical process. (b)–(d) The spatial densities of the NM $\langle \hat{n}_N^{\alpha} \rangle$ (blue circles), the kink $\langle \hat{n}_K^{\tilde{\alpha}} \rangle$ (red diamonds), and the antikink $\langle \hat{n}_A^{\tilde{\alpha}} \rangle$ (purple triangles) at (b) the beginning and (c) and (d) later times marked by gray vertical lines in (a).

IV. DISCUSSION AND OUTLOOK

Ultracold atoms have become an important platform for quantum simulation and allow us to implement various atomic pseudospin models. The latter enabled the simulation of different magnetic quasiparticles, such as magnons [23], spin and magnetic polarons [27,28], spinons [24], and kinks [29,30,34], as well as the monopole [36–40]. Existing simulations have mainly focused on the excitation condition and the dynamical properties of quasiparticles of an individual type. The DSG pseudospin system allows, however, for the coexistence and coupling, i.e., interaction effects, of the magnetic monopole and kink, which enriches the previously investigated scenario of the quantum simulation of individual magnetic quasiparticles with ultracold atoms.

The key ingredients of the DSG pseudospin scheme involve the double-well superlattice and the dipolar interaction, which are realizable within current experimental techniques. The double-well superlattice is typically realized by the superposition of two pairs of counterpropagating laser beams [54–57], with $\lambda_1 = 2\lambda_2$, where $\lambda_{1(2)}$ refer to the wavelengths of the laser beams. Dipolar quantum gases can be composed of ultracold polar atoms [58,59], Rydberg atoms [60,61], and polar molecules [62,63]. In particular, our numerical simulations truncated the dipolar interaction to the nearest-neighbor interaction, which can be implemented by, e.g., the Rydberg dressing [64,65]. (An estimation of the experimental parameters is given in Appendix E.) Moreover, this simulation scheme can be directly generalized to two-dimensional superlattice potentials, which not only generalizes the spin chain to the two-dimensional square [66] and triangular lattices [54,67] but also enables the simulation of Dzyaloshinskii-Moriya-like spin-spin interactions by exploring the anisotropy of the dipolar interaction.

Based on our simulation scheme, we have revealed binding and antibinding effects between the monopole and the kink. These effects are not restricted to the case of ultracold atomic pseudospins and can be generalized to condensed-matter spin systems. It is interesting to note that a very recent experimental work investigating CoTb films [68] reported the excitation of magnetic monopole pairs, in which the excited monopole pairs are bound to a ferromagnetic domain wall, i.e., the two-dimensional counterpart of the magnetic kink. The binding effect in both the pseudospin and condensed-matter spin systems can be attributed to the common nature of the singular magnetic field of the monopole exerted on neighboring spins, which induces the attractive interaction between the monopole and the kink or domain wall. It can also be expected that a simulation based on ultracold quantum gases would stimulate related investigations in (artificial) spin lattices [69,70].

ACKNOWLEDGMENTS

The authors would like to acknowledge T. Shi and Y. Chang for inspiring discussions, as well as Y. Cai for the helpful discussion on the experimental realization of the Rydberg dressing. This work was supported by the National Natural Science Foundation of China (Grants No. 11625417, No. 11604107, No. 91636219, and No. 11727809) and the Cluster of Excellence "Advanced Imaging of Matter" of the Deutsche Forschungsgemeinschaft (DFG), EXC 2056, Project ID No. 390715994.

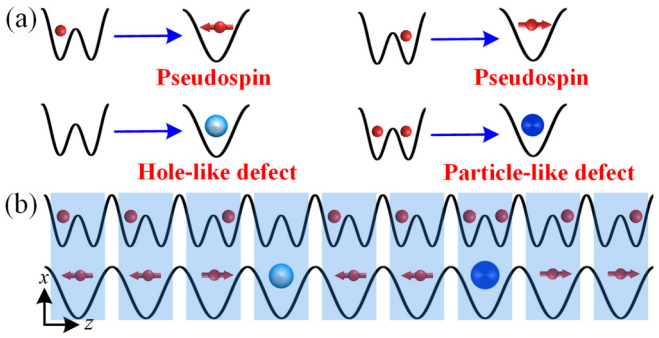

FIG. 5. Illustration of the pseudospin mapping. (a) The occupation states of the arbitrary cell are mapped to the pseudospin and defect states. (b) The original DSG system (top panel) and the effective doped pseudospin chain (bottom panel).

APPENDIX A: THE PSEUDOSPIN MAPPING

In this Appendix, a more visualizable demonstration of the pseudospin mapping is provided in Fig. 5. As introduced in the main text, there are four single-cell occupation states, $\{|1,0\rangle_i, |0,1\rangle_i, |1,1\rangle_i, |0,0\rangle_i\}$, each of which is mapped to a spin state and/or defect state. The mapping of the four occupation states to the corresponding spin and/or defect states is given in Fig. 5(a). Following the pseudospin mapping, the whole superlattice loaded with atoms can be mapped to a spin chain with doped NM and SM, and the mapping between the superlattice of a particular atom-filling configuration and the corresponding doped spin chain is shown in Fig. 5(b).

APPENDIX B: THE POLARIZATION EFFECT OF THE MONOPOLE

Here, we provide more calculation results for the spin-polarization effect of the NM and SM, which are compared to the spin polarization induced by a normal magnetic defect. To accomplish this, we consider a transverse Ising spin chain doped with a defect localized in the middle of the chain. Without the doping, the spins in the chain are all aligned in the x direction by the transverse magnetic field, and the spin chain resides in the paramagnetic phase. The doped defect can interact with its neighboring spins and can polarize these spins in a "new" direction. Defects of different types can result in very different spin textures of the neighboring spins. Here, we separately consider three types of defects, namely, the NM, the SM, and a normal magnetic defect, and compare the spin textures from these defects. We model the normal magnetic defect as a particle of $1/2$ spin, and the spin state of the defect is fixed to $|\uparrow\rangle_z$.

In our study, the Hamiltonian is taken as $\hat{H} = \hat{H}_0 + \hat{H}^{\alpha}_{\text{defect}}$, where $\hat{H}_0$ refers to the Hamiltonian of the transverse Ising spin chain, as introduced in the main text. $\hat{H}^{\alpha}_{\text{defect}}$ corresponds to the spin-defect interaction, with $\alpha =$ NM, SM, and normal,

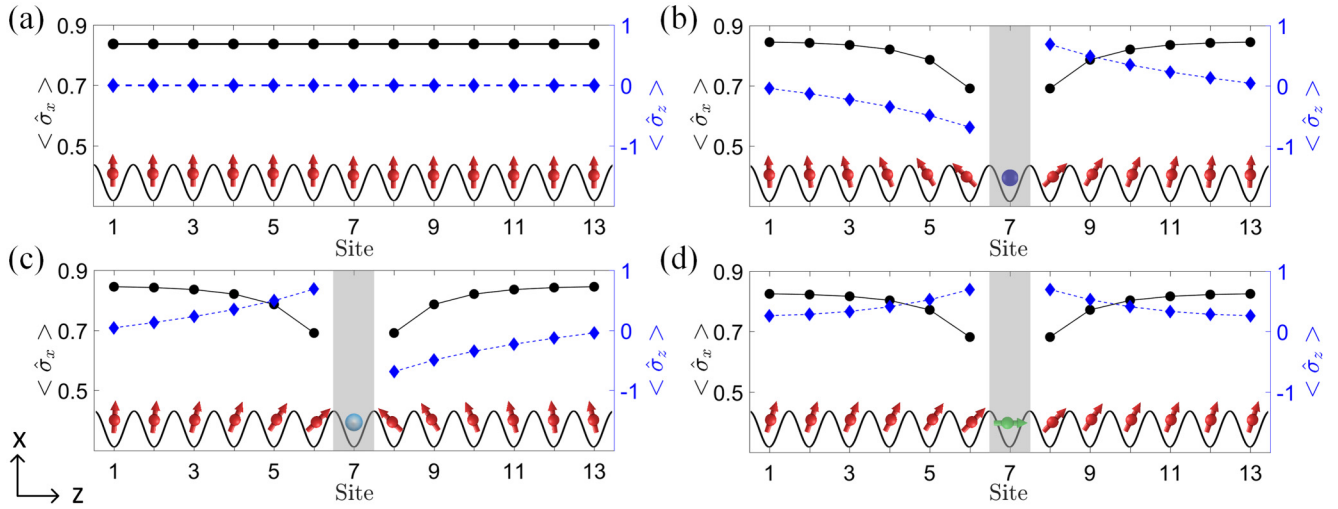

FIG. 6. The polarization effect for different defects for $d = 3J$. (a) The magnetization along the x (black) and z (blue) axes of the undoped spin chain. (b) The NM, (c) SM, and (d) normal magnetic defect cases. The black solid circles and blue diamonds represent $\langle\hat{\sigma}_x\rangle$ and $\langle\hat{\sigma}_z\rangle$, respectively.

denoting the NM, SM, and normal magnetic defects. The different spin-defect interactions read

$$\hat{H}_{\text{defect}}^{\text{NM}} = \frac{d}{4}\sum_{\alpha}^{M}\hat{n}_N^{\alpha}\left(\hat{\sigma}_z^{\alpha-1} - \hat{\sigma}_z^{\alpha+1}\right), \tag{B1a}$$

$$\hat{H}_{\text{defect}}^{\text{SM}} = \frac{d}{4}\sum_{\alpha}^{M}\hat{n}_S^{\alpha}\left(-\hat{\sigma}_z^{\alpha-1} + \hat{\sigma}_z^{\alpha+1}\right), \tag{B1b}$$

$$\hat{H}_{\text{defect}}^{\text{normal}} = \frac{d}{4}\sum_{\alpha}^{M}\hat{n}_{\text{nor}}^{\alpha}\left(-\hat{\sigma}_z^{\alpha-1} - \hat{\sigma}_z^{\alpha+1}\right). \tag{B1c}$$

$\hat{H}_{\text{defect}}^{\text{normal}}$ is taken from the case of, for instance, doping magnetic atoms to electron gases, where the doped atom plays the role of the normal magnetic defect. The results are shown in Fig. 6. Figure 6(a) shows the spin polarization of the undoped DSG spin chain in the weak interaction regime ($d = 3J$), which corresponds to the paramagnetic phase. In Figs. 6(b) and 6(c), we present the results for the NM and SM defects. Here, we observe that the neighboring spins point away from (towards) the NM (SM) defect. Figure 6(d) provides a comparison to the normal magnetic defect, which polarizes the neighboring spins on its left and right sides in the same direction.

APPENDIX C: THE SQUEEZED SPACE

In this section, we use Fig. 7 to give a more explicit demonstration of the basis defined in the squeezed space. Figure 7(a) shows one of the basis states of the pseudospin chain with nine spins labeled $\alpha = 1$–9. Two kinks and an antikink are located between sites (2, 3), (8, 9), and (6, 7). The basis with a doped particle defect on the fifth site is shown in Fig. 7(b). Subsequently, we remove the particle defect from the pseudospin chain, and the left spins [Fig. 7(c)] form the squeezed space. The spins on the right side of the particle defect are squeezed forward. The left spins in the squeezed space are relabeled $\tilde{\alpha} = 1$–8, where $\tilde{\alpha} = \alpha$ and $\tilde{\alpha} = \alpha + 1$ for $\alpha < 5$ and $\alpha > 5$, respectively. In the squeezed space, the kinks and antikink are located between sites (2, 3), (7, 8), and (5, 6). The falling and rising edges of the purple solid line in Fig. 7(d) indicate the positions of kinks and antikink, respectively.

APPENDIX D: CALCULATIONS OF THE DYNAMICAL STRUCTURE FACTOR

In this Appendix, we present two approaches to calculate the dynamical structure factor. The first approach is based on [1], in which $S(k, \omega)$ is determined using the Fourier transformation of the time-dependent correlation function. The second approach, following the proposal in [46], couples the DSG system to a particle bath and applies a periodic variation of the coupling strength. Then $S(k, \omega)$ is extracted from the dynamical process under periodic driving, which resembles the angle-resolved photoemission spectroscopy (ARPES) signal. The two approaches give qualitatively the same results, and the main difference arises from the quantitative weights of each mode. Given the comparison between the two

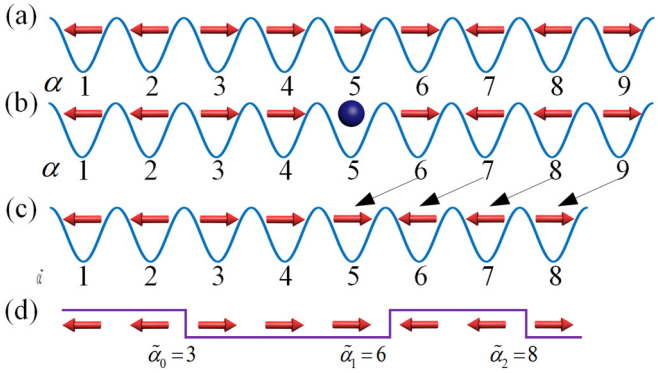

FIG. 7. Illustration of squeezed space. (a) The basis without defects. (b) The basis with the single-particle defect at the fifth site. (c) The basis in a squeezed space. (d) The kink-antikink basis.

approaches, we show the results of the first approach in Fig. 2(a) in the main text.

First, we provide the definition of the single-particle spectral function, which is the imaginary part of the single-particle retarded Green's function. The single-particle retarded Green's function $G^R(k,t)$ in the Lehmann representation at zero temperature reads [71]

$$G^R(k,\omega)=\sum_{n,\sigma}\left\{\frac{\left|\langle\psi_n|\hat{a}^\dagger_{k,\sigma}|\varphi_0\rangle\right|^2}{\omega+\varepsilon_0-\varepsilon_n+i\eta}+\frac{|\langle\psi_n|\hat{a}_{k,\sigma}|\varphi_0\rangle|^2}{\omega-\varepsilon_0+\varepsilon_n+i\eta}\right\}, \tag{D1}$$

where $\hat{a}^\dagger_{k,\sigma}=\sqrt{2/(M+1)}\sum_{j=1}^{M}\sin[kj/(M+1)]\hat{a}^\dagger_{j,\sigma}$ creates a fermion with momentum k and spin σ. $|\varphi_0\rangle$ is the ground state of the system without doping, and $|\psi_n\rangle$ is the nth eigenstate of the system with single-particle doping, while ε_0 and ε_n are their energies. $\eta\in\mathbb{R}^+$, and we consider the limit $\eta\to 0^+$. We focus on the single-particle excitations, and we therefore have $|\langle\psi_n|\hat{a}_{k,\sigma}|\varphi_0\rangle|^2=0$. The single-particle spectral function $S(k,\omega)$ takes on the following appearance:

$$\begin{aligned}S^G(k,\omega)&=-\frac{1}{\pi}\mathrm{Im}\{G^R(k,\omega)\}\\&=\sum_{n,\sigma}|\langle\psi_n|\hat{a}^\dagger_{k,\sigma}|\varphi_0\rangle|^2\delta(\omega+\varepsilon_0-\varepsilon_n),\end{aligned} \tag{D2}$$

and the density of states (DOS) is defined as $\rho^G(\omega)=\int dkS^G(k,\omega)$.

1. Approach 1

Following Eq. (A1) in Ref. [47], the approach first determines the spin-spin time-dependent correlation function, which is defined as

$$C(i,t)=\sum_{\sigma}\langle\varphi_0|e^{i\hat{H}t}\hat{a}_{i,\sigma}e^{-i\hat{H}t}\hat{a}^\dagger_{1,\sigma}|\varphi_0\rangle, \tag{D3}$$

where $\hat{a}^\dagger_{i,\to/\leftarrow}/\hat{a}_{i,\to/\leftarrow}=\hat{f}^\dagger_{2i/2i-1}/\hat{f}_{2i/2i-1}$ is the fermionic creation (annihilation) operator of the right (left) site of the ith supercell. Then the spatial Fourier transform is performed and gives rise to

$$A(k,t)=\sqrt{\frac{2}{M+1}}\sum_i\sin\left(\frac{ik}{M+1}\right)C(i,t). \tag{D4}$$

Finally, the dynamical structure factor $S^F(k,\omega)$ is obtained with the Fourier transformation in time:

$$S^F(k,\omega)=\frac{1}{2\pi}\int_{-\infty}^{\infty}dtA(k,t), \tag{D5}$$

and the DOS is given by $\rho^F(\omega)=\int dkS^F(k,\omega)$.

2. Approach 2

The second approach involves the simulation of the ARPES process [46]. In the simulation of ARPES, the undoped DSG system is first connected to a bath system, which allows particle hopping between the DSG chain and the bath. Periodic shaking is then applied to the coupling strength with a particular shaking frequency. During the dynamical process under the shaking, particles can tunnel from the bath to the DSG chain, corresponding to the doping of a particle to the DSG system. The structure factor is then associated with the momentum distribution of the hole in the bath at the particular driving frequency. We illustrate our simulation setup of this ARPES process as follows: First, we consider the DSG+bath system in Fig. 8, in which the bath is a lattice of atoms in the Mott state. The lattice of the bath system has the same period as the double-well superlattice, but there is a single site per cell. We load the same spin-polarized fermions into the DSG system and the bath system, while the DSG and bath systems are half and unit filling, respectively.

The Hamiltonian of the DSG+bath system reads

$$\hat{H}_{\mathrm{DSG+bath}}=\hat{H}_{\mathrm{DSG}}+\hat{H}_{\mathrm{bath}}+\hat{H}_{\mathrm{intra}}, \tag{D6a}$$

$$\begin{aligned}\hat{H}_{\mathrm{DSG}}=&-J\sum_{i=1}^{M}(\hat{f}^\dagger_{2i}\hat{f}_{2i-1}+\mathrm{H.c.})\\&-J_1\sum_{i=1}^{M-1}(\hat{f}^\dagger_{2i}\hat{f}_{2i+1}+\mathrm{H.c.})\\&+\sum_{i<j\in[1,2M]}^{M-1}V_d(j-i)\hat{n}_i\hat{n}_j,\end{aligned} \tag{D6b}$$

$$\hat{H}_{\mathrm{bath}}=-J_0\sum_{i=1}^{M}(\hat{c}^\dagger_i\hat{c}_{i-1}+\mathrm{H.c.})+\Delta\sum_{i=1}^{M-1}\tilde{n}_i, \tag{D6c}$$

$$\hat{H}_{\mathrm{inter}}=-J_{\mathrm{inter}}\sin(\omega_S t)\sum_{i=1}^{M}[\hat{c}^\dagger_i(\hat{f}_{2i-1}+\hat{f}_{2i})+\mathrm{H.c.}], \tag{D6d}$$

where $\hat{f}^\dagger_{2i/2i-1}$ and $\hat{f}_{2i/2i-1}$ ($\hat{c}^\dagger_i$ and $\hat{c}_i$) are the fermionic creation and annihilation operators, respectively, of the right and left sites of the ith supercell (cell) in the DSG (bath) system and the operator $\hat{n}_i=\hat{f}^\dagger_i\hat{f}_i$ ($\tilde{n}_i=\hat{c}^\dagger_i\hat{c}_i$) counts the number of fermions in site i in the DSG (bath) system. The first two terms in $\hat{H}_{\mathrm{DSG}}$ describe the intra- and intercell hoppings, respectively, with hopping amplitudes J and J_1. Δ is the offset of the bath relative to the DSG, and the hopping amplitude of the fermions in the bath is J_0. The dipole-dipole interaction (DDI) between two fermions located in the ith and jth sites is taken to be $V_d(j-i)=d/|x_j-x_i|^3$, where x_i (x_j) is the local minimum of the corresponding site and d denotes the DDI strength. In the bath system, the fermions are well separated from each other, and we therefore ignore the DDI among them. The lattice modulation can be described by $\hat{H}_{\mathrm{inter}}$, and $J_{\mathrm{inter}}\ll J_1$ is the perturbation term.

$\hat{H}_{\mathrm{inter}}$ induces hopping of atoms from the bath to the DSG system, and the energy change in the DSG system due to the doping is $\hbar\omega=E^{M+1}-E^M$ for single-atom hopping. For lattice modulation frequency ω_S, this is determined by the energy conservation:

$$\hbar\omega=\hbar\omega_S-E^B(k)-\Delta, \tag{D7}$$

where $E^B(k)=-2J_0\cos(k)$ is the energy of the hole in the bath system. The offset Δ is taken to be $8d$ and $9d$ when we detect the dynamical structure factors of the first and second bands, corresponding to the energy of a NM and the energy of one NM and antikink, respectively. The momentum and

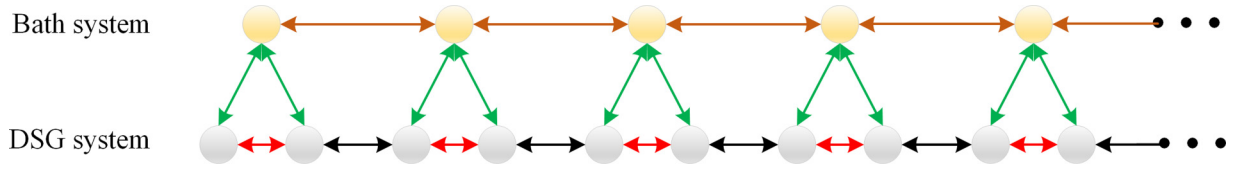

FIG. 8. The proposed setup. The red (black) arrows indicate the intracell (intercell) hopping of spin-polarized fermions in the DSG system. The brown arrows indicate the hopping of fermions in the bath, while the green arrows are the modulation between these two systems.

energy resolution spectrum function are obtained by detecting the momentum distribution of the hole for different ω_S.

The structure factor $S^M(k,\omega_S)$ is determined from the reduced density matrix of the hole in the bath system as

$$S^M(k,\omega_S)=\frac{\hbar}{2\pi J_0^2}\Gamma(k,\omega_S), \tag{D8}$$

where $\Gamma(k,\omega_S)=\frac{1}{M+1}\sum_{i,j}\sin(ik)\sin(jk)R_{\omega_S}(i,j)$ is the probability of creating a particle with momentum k and energy $\hbar\omega_S$. $R_{\omega_S}(i,j)=\mathrm{tr}_{\mathrm{DSG}}[|\psi(t_{\omega_S})\rangle\langle\psi(t_{\omega_S})|]$ is the reduced density matrix of the hole in the bath, while $|\psi(t_{\omega_S})\rangle$ is the wave function of the complete system at t_{ω_S}. At $t=t_{\omega_S}$, the probability of the $\mathrm{tr}[R_{\omega_S}(i,j)]$ hole takes a maximum for a given shaking with frequency ω_S. The DOS is naturally defined as $\rho^M(\omega)=\int dk S^M(k,\omega)$.

In the strong-interaction regime, which is of interest here, the gap between the adjacent bands is much larger than the strength of shaking. As a result, we need to take only the resonant states into account. For a certain ω_S, after transforming to the rotating frame and performing a rotating-wave approximation, one obtains the Hamiltonians

$$\hat{H}^{\mathrm{RWA}}=\hat{H}_{\mathrm{DSG}}+\hat{H}^{\mathrm{RWA}}_{\mathrm{bath}}+\hat{H}^{\mathrm{RWA}}_{\mathrm{inter}}, \tag{D9a}$$

$$\hat{H}_{\mathrm{DSG}}=-J\sum_{i=1}^{M}(\hat{f}^{\dagger}_{2i}\hat{f}_{2i-1}+\mathrm{H.c.})-J_1\sum_{i=1}^{M-1}(\hat{f}^{\dagger}_{2i}\hat{f}_{2i+1}+\mathrm{H.c.})+\sum_{i<j\in[1,2M]}^{M-1}V_d(j-i)\hat{n}_i\hat{n}_j, \tag{D9b}$$

$$\hat{H}^{\mathrm{RWA}}_{\mathrm{bath}}=-J_0\sum_{i=1}^{M}(\hat{c}^{\dagger}_i\hat{c}_{i-1}+\mathrm{H.c.})+(\Delta-\omega_S)\sum_{i=1}^{M-1}\tilde{n}_i, \tag{D9c}$$

$$\hat{H}^{\mathrm{RWA}}_{\mathrm{inter}}=-\frac{J_{\mathrm{inter}}}{2}\sum_{i=1}^{M}[\hat{c}^{\dagger}_i(\hat{f}_{2i-1}+\hat{f}_{2i})+\mathrm{H.c.}]. \tag{D9d}$$

Throughout our numerical calculation, we set $J=1$ as the unit. The other parameters are $J_0=J_1=0.1$, $d=40$, $J_{\mathrm{inter}}=0.01$, and the evolution time $T=1000$.

The structure factors computed with the first and second approaches are given in Figs. 9(a) and 9(b) with $S^F(k,\omega)$ and $S^M(k,\omega)$, respectively. We omit the frequency interval of $\omega\in(0.5,35)$ as $S^{F/M}(k,\omega)\sim 0$, which is the gap between the first two bands. $S^X(k,\omega)$ is normalized to unity $\int d\omega S^X(k,\omega)=1$, with $X=F,M,G$ [72]. $S^F(k,\omega)$ and $S^M(k,\omega)$ are qualitatively the same, although it looks like there are more details in Fig. 9(b). This is confirmed by the DOS shown in Figs. 9(c) and 9(d). Figure 9(c) shows $\rho^G(\omega)$ (purple), $\rho^F(\omega)$ (blue), and $\rho^M(\omega)$ (red) for $\omega\in[-0.5,0.5]$, and their peaks locate at the same position with similar amplitudes. In Fig. 9(d), we show the DOS for $\omega\in[-35,45]$. The peaks almost match, although $\rho^F(\omega)$ is invisible for the higher excited states of the second band. This is because $|\langle\psi_n|\hat{c}^{\dagger}_{k,\sigma}|\varphi_0\rangle|^2\sim 0$ for these higher excited states. The most direct way to improve the intensity of $S^F(k,\omega)$ is to take the rest of the eigenstates of the undoped system into account.

The above analysis compares different approaches to obtain the dynamical structure factor, which give qualitatively the same spectrum, with the difference mainly arising in the quantitative amplitude of each mode. We then adapt the first

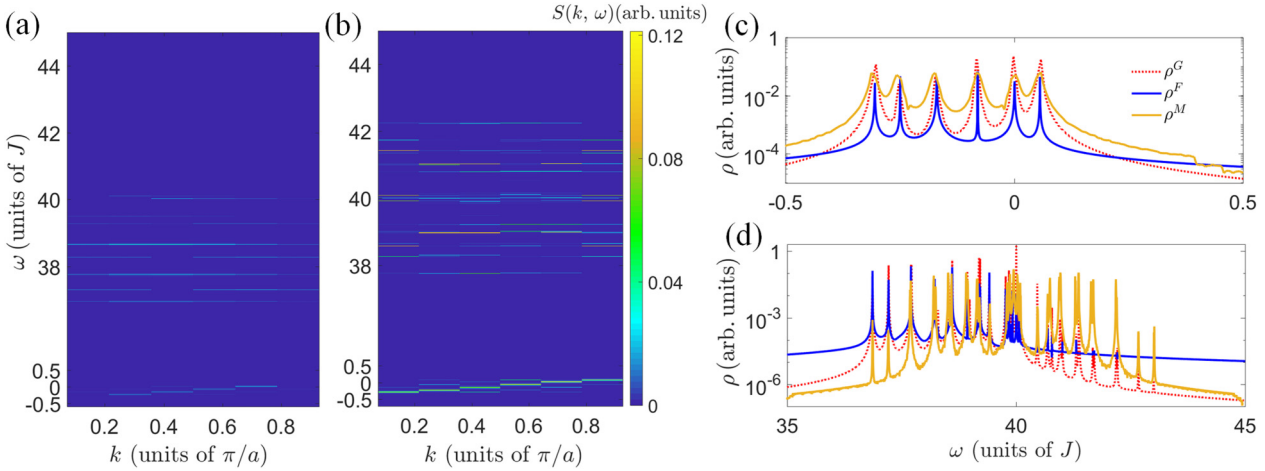

FIG. 9. Dynamical structure factor of the six-site DSG pseudospin chain. (a) $S^F(k,\omega)$ obtained with the Fourier transform of the time-dependent correlation function. (b) $S^M(k,\omega)$ originating from the lattice modulation. (c) and (d) The DOSs with ρ^G (red dashed line), ρ^F (blue solid line), and ρ^M (orange solid line).

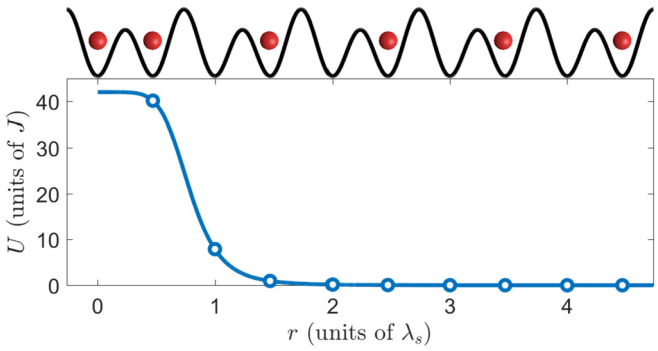

FIG. 10. The interaction strength versus the relative distance between atoms, in units of J and λ_s, respectively. The panel above plots the double-well superlattice with the same length scale as the relative distance in the main plot to demonstrate that the interaction mainly affects atoms that are nearest neighbors.

approach since it is more setup independent and does not rely on the setting of, e.g., the bath.

APPENDIX E: THE EXPERIMENTAL REALIZATION

Here, we discuss the experimental realizability of the DSG simulation scheme. The key ingredients of our scheme involve the double-well superlattice and the dipolar interaction, which are realizable within the current experimental techniques. The double-well superlattice is typically realized by the superposition of two pairs of counterpropagating laser beams [54–57]. The dipolar quantum gases can be composed of ultracold polar atoms [58,59], Rydberg atoms [60,61], and polar molecules [62,63]. In particular, our numerical simulations truncated the dipolar interaction to the nearest-neighbor interaction, which can be implemented by, e.g., the Rydberg dressing [64,65]. The DSG simulation scheme also requires $U \gg J \gg J_1$, where U, J, and J_1 denote the strength of the nearest-neighbor (NN) interaction as well as the intra- and intercell hoppings. In our numerical simulation, we take the parameters $U = 40J = 400J_1$, where the DSG pseudospin chain resides in the single-kink phase.

Taking ^{6}Li atoms as the working medium, the wavelengths for the laser beams to form the double-well superlattice are $\lambda_s = 2.3\ \mu$m and $\lambda_l = 2\lambda_s$. Fixing the amplitudes of the lattice height of the short- and long-wavelength lattices as $V_s = 18E_R$, $V_l = 6.2E_R$ leads to intra- and intercell hopping strengths of $J = 10J_1 = 68$ Hz, where $E_R = h^2/(2\lambda_s^2 m_{Li})$ is the recoil energy, with h and m_{Li} denoting the Planck constant and the atomic mass.

The NN interaction can be induced by the Rydberg dressing, and we take the Rydberg state to be $|34S_{1/2}\rangle$ for demonstration, with the van der Waals–type interaction coefficient $C_6 = 46.5$ MHz μm^6. To be consistent with the double-well superlattice settings, the NN interaction strength should take the value $U = 2.72$ kHz, with the Rydberg radius approaching the period length of the lattice. It can be found that choosing the detuning and Rabi frequency of the Rydberg excitation laser to be 43.8 and 6.6 MHz leads to $U \sim 2.72$ kHz and Rydberg radius $R_c = 0.9\ \mu$m, which meets the requirement of the setting of our numerical simulations. We plot the interaction strength as a function of the relative distance between atoms in Fig. 10 to visualize the NN interaction induced by the Rydberg dressing, and this interaction fulfills the DSG simulation scheme.

It is also worth mentioning that the simulation scheme is flexible with respect to the choice of parameters and can be implemented over a wide parameter regime, enabling a feasible experimental realization.

[1] F. C. Alcaraz, S. R. Salinas, and W. F. Wreszinski, Phys. Rev. Lett. **75**, 930 (1995).
[2] S. B. Rutkevich, J. Stat. Mech. **2010**, P07015.
[3] M. Mourigal, M. Enderle, A. Klöpperpieper, J. S. Caux, A. Stunault, and H. M. Rønnow, Nat. Phys. **9**, 435 (2013).
[4] F. Ferrari and F. Becca, Phys. Rev. X **9**, 031026 (2019).
[5] S. Gao, H. D. Rosales, F. A. G. Albarracín, V. Tsurkan, G. Kaur, T. Fennell, P. Steffens, M. Boehm, P. Čermák, A. Schneidewind, E. Ressouche, D. C. Cabra, C. Rüegg, and O. Zaharko, Nature (London) **586**, 37 (2020).
[6] N. C. Randeep and N. Surendran, Phys. Rev. B **100**, 045134 (2019).
[7] C. Castelnovo, R. Moessner, and S. L. Sondhi, Nature (London) **451**, 42 (2008).
[8] L. D. C. Jaubert and P. C. W. Holdsworth, Nat. Phys. **5**, 258 (2009).
[9] T. Fennell, P. P. Deen, A. R. Wildes, K. Schmalzl, D. Prabhakaran, A. T. Boothroyd, R. J. Aldus, D. F. McMorrow, and S. T. Bramwell, Science **326**, 415 (2009).
[10] D. J. P. Morris, D. A. Tennant, S. A. Grigera, B. Klemke, C. Castelnovo, R. Moessner, C. Czternasty, M. Meissner, K. C. Rule, J.-U. Hoffmann, K. Kiefer, S. Gerischer, D. Slobinsky, and R. S. Perry, Science **326**, 411 (2009).
[11] D. A. Allwood, G. Xiong, C. C. Faulkner, D. Atkinson, D. Petit, and R. P. Cowburn, Science **309**, 1688 (2005).
[12] S. S. P. Parkin, M. Hayashi, and L. Thomas, Science **320**, 190 (2008).
[13] P. Yan and G. E. W. Bauer, Phys. Rev. Lett. **109**, 087202 (2012).
[14] H. Zhang, Z. Zhao, D. Gautreau, M. Raczkowski, A. Saha, V. O. Garlea, H. Cao, T. Hong, H. O. Jeschke, S. D. Mahanti, T. Birol, F. F. Assaad, and X. Ke, Phys. Rev. Lett. **125**, 037204 (2020).
[15] A. Keselman, L. Balents, and O. A. Starykh, Phys. Rev. Lett. **125**, 187201 (2020).
[16] R. Hertel, W. Wulfhekel, and J. Kirschner, Phys. Rev. Lett. **93**, 257202 (2004).
[17] J. Iwasaki, A. J. Beekman, and N. Nagaosa, Phys. Rev. B **89**, 064412 (2014).
[18] C. Schütte and M. Garst, Phys. Rev. B **90**, 094423 (2014).
[19] Z. Wang, H. Y. Yuan, Y. Cao, Z.-X. Li, R. A. Duine, and P. Yan, Phys. Rev. Lett. **127**, 037202 (2021).
[20] C. Gross and I. Bloch, Science **357**, 995 (2017).

[21] R. E. Barfknecht, A. Foerster, and N. T. Zinner, Phys. Rev. A **95**, 023612 (2017).

[22] F. Deuretzbacher, D. Becker, J. Bjerlin, S. M. Reimann, and L. Santos, Phys. Rev. A **95**, 043630 (2017).

[23] T. Fukuhara, P. Schauß, M. Endres, S. Hild, M. Cheneau, I. Bloch, and C. Gross, Nature (London) **502**, 76 (2013).

[24] J. Vijayan, P. Sompet, G. Salomon, J. Koepsell, S. Hirthe, A. Bohrdt, F. Grusdt, I. Bloch, and C. Gross, Science **367**, 186 (2020).

[25] A. Mazurenko, C. S. Chiu, G. Ji, M. F. Parsons, M. K. Nagy, R. Schmidt, F. Grusdt, E. Demler, D. Greif, and M. Greiner, Nature (London) **545**, 462 (2017).

[26] E. Kuznetsova, S. T. Rittenhouse, I. I. Beterov, M. O. Scully, S. F. Yelin, and H. R. Sadeghpour, Phys. Rev. A **98**, 043609 (2018).

[27] J. Koepsell, J. Vijayan, P. Sompet, F. Grusdt, T. A. Hilker, E. Demler, G. Salomon, I. Bloch, and C. Gross, Nature (London) **572**, 358 (2019).

[28] C. S. Chiu, G. Ji, A. Bohrdt, M. Xu, M. Knap, E. Demler, F. Grusdt, M. Greiner, and D. Greif, Science **365**, 2516 (2019).

[29] F. Liu, R. Lundgren, P. Titum, G. Pagano, J. Zhang, C. Monroe, and A. V. Gorshkov, Phys. Rev. Lett. **122**, 150601 (2019).

[30] W. L. Tan, P. Becker, F. Liu, G. Pagano, K. S. Collins, A. De, L. Feng, H. B. Kaplan, A. Kyprianidis, R. Lundgren, W. Morong, S. Whitsitt, A. V. Gorshkov, and C. Monroe, Nat. Phys. **17**, 742 (2021).

[31] J. Simon, W. S. Bakr, R. Ma, M. E. Tai, P. M. Preiss, and M. Greiner, Nature (London) **472**, 307 (2011).

[32] J. R. Li, W. Huang, B. Shteynas, F. Ç. Top, E. Su, J. Lee, A. O. Jamison, and W. Ketterle, Phys. Rev. Lett. **117**, 185301 (2016).

[33] J. R. Li, J. Lee, W. Huang, S. Burchesky, B. Shteynas, F. Ç. Top, A. O. Jamison, and W. Ketterle, Nature (London) **543**, 91 (2017).

[34] X. Yin, L. Cao, and P. Schmelcher, Europhys. Lett. **110**, 26004 (2015).

[35] L. Cao, S. I. Mistakidis, X. Deng, and P. Schmelcher, Chem. Phys. **482**, 303 (2017).

[36] V. Pietilä and M. Möttönen, Phys. Rev. Lett. **103**, 030401 (2009).

[37] V. Pietilä and M. Möttönen, Phys. Rev. Lett. **102**, 080403 (2009).

[38] M. W. Ray, E. Ruokokoski, S. Kandel, M. Möttönen, and D. S. Hall, Nature (London) **505**, 657 (2014).

[39] M. W. Ray, E. Ruokokoski, K. Tiurev, M. Möttönen, and D. S. Hall, Science **348**, 544 (2015).

[40] S. Sugawa, F. S. Carcoba, A. R. Perry, Y. Yue, and I. B. Spielman, Science **360**, 1429 (2018).

[41] T. Lahaye, C. Menotti, L. Santos, M. Lewenstein, and T. Pfau, Rep. Prog. Phys. **72**, 126401 (2009).

[42] R. Schilling, Phys. Rev. B **15**, 2700 (1977).

[43] K. T. Bach and N. Macris, Phys. A (Amsterdam, Neth.) **279**, 386 (2000).

[44] F. C. Alcaraz, A. Saguia, and M. S. Sarandy, Phys. Rev. A **70**, 032333 (2004).

[45] T. A. Hilker, G. Salomon, F. Grusdt, A. Omran, M. Boll, E. Demler, I. Bloch, and C. Gross, Science **357**, 484 (2017).

[46] A. Bohrdt, D. Greif, E. Demler, M. Knap, and F. Grusdt, Phys. Rev. B **97**, 125117 (2018).

[47] A. Bohrdt, E. Demler, F. Pollmann, M. Knap, and F. Grusdt, Phys. Rev. B **102**, 035139 (2020).

[48] L. Cao, S. Krönke, O. Vendrell, and P. Schmelcher, J. Chem. Phys. **139**, 134103 (2013).

[49] S. Krönke, L. Cao, O. Vendrell, and P. Schmelcher, New J. Phys. **15**, 063018 (2013).

[50] L. Cao, V. Bolsinger, S. I. Mistakidis, G. M. Koutentakis, S. Krnke, J. M. Schurer, and P. Schmelcher, J. Chem. Phys. **147**, 044106 (2017).

[51] Y. Wang, A. Bohrdt, S. Ding, J. Koepsell, E. Demler, and F. Grusdt, Phys. Rev. Research **3**, 033204 (2021).

[52] F. Grusdt, M. K. Nagy, A. Bohrdt, C. S. Chiu, G. Ji, M. Greiner, D. Greif, and E. Demler, Phys. Rev. X **8**, 011046 (2018).

[53] S. I. Mistakidis, A. G. Volosniev, N. T. Zinner, and P. Schmelcher, Phys. Rev. A **100**, 013619 (2019).

[54] J. Sebby-Strabley, M. Anderlini, P. S. Jessen, and J. V. Porto, Phys. Rev. A **73**, 033605 (2006).

[55] S. Fölling, S. Trotzky, P. Cheinet, M. Feld, R. Saers, A. Widera, T. Mller, and I. Bloch, Nature (London) **448**, 1029 (2007).

[56] M. Anderlini, P. J. Lee, B. L. Brown, J. S. Strabley, W. D. Phillips, and J. V. Porto, Nature (London) **448**, 452 (2007).

[57] H. N. Dai, B. Yang, A. Reingruber, X. F. Xu, X. Jiang, Y. A. Chen, Z. S. Yuan, and J. W. Pan, Nat. Phys. **12**, 783 (2016).

[58] Y. Li, W. Pang, J. Xu, C. Lee, B. A. Malomed, and L. Santos, New J. Phys. **19**, 013030 (2017).

[59] T. Ollikainen, K. Tiurev, A. Blinova, W. Lee, D. S. Hall, and M. Möttönen, Phys. Rev. X **7**, 021023 (2017).

[60] D. W. Schönleber, A. Eisfeld, M. Genkin, S. Whitlock, and S. Wüster, Phys. Rev. Lett. **114**, 123005 (2015).

[61] T. L. Nguyen, J. M. Raimond, C. Sayrin, R. Cortiñas, T. Cantat-Moltrecht, F. Assemat, I. Dotsenko, S. Gleyzes, S. Haroche, G. Roux, Th. Jolicoeur, and M. Brune, Phys. Rev. X **8**, 011032 (2018).

[62] A. Micheli, G. K. Brennen, and P. Zoller, Nat. Phys. **2**, 341 (2006).

[63] T. Schuster, F. Flicker, M. Li, S. Kotochigova, J. E. Moore, J. Ye, and N. Y. Yao, Phys. Rev. Lett. **127**, 015301 (2021).

[64] J. Zeiher, R. Bijnen, P. Schauß, S. Hild, J. Y. Choi, T. Pohl, I. Bloch, and C. Gross, Nat. Phys. **12**, 1095 (2016).

[65] J. Zeiher, J. Y. Choi, A. Rubio-Abadal, T. Pohl, R. van Bijnen, I. Bloch, and C. Gross, Phys. Rev. X **7**, 041063 (2017).

[66] B. Yang, H. Sun, C. J. Huang, H. Y. Wang, Y. Deng, H. N. Dai, Z. S. Yuan, and J.-W. Pan, Science **369**, 550 (2020).

[67] P. J. Lee, M. Anderlini, B. L. Brown, J. Sebby-Strabley, W. D. Phillips, and J. V. Porto, Phys. Rev. Lett. **99**, 020402 (2007).

[68] Y. Guang, K. Ran, J. Zhang, Y. Liu, S. Zhang, X. Qiu, Y. Peng, X. Zhang, M. Weigand, J. Gräfe, G. Schütz, G. van der Laan, T. Hesjedal, S. Zhang, G. Yu, and X. Han, Phys. Rev. Lett. **127**, 217201 (2021).

[69] A. D. King, C. Nisoli, E. D. Dahl, G. P. Lamarre, and A. L. Bezanilla, Science **373**, 576 (2021).

[70] A. Farhan, M. Saccone, C. F. Petersen, S. Dhuey, R. V. Chopdekar, Y. L. Huang, N. Kent, Z. Chen, M. J. Alava, T. Lippert, A. Scholl, and S. V. Dijken, Sci. Adv. **5**, eaav6380 (2019).

[71] A. Damascelli, Phys. Scr. **T109**, 61 (2004).

[72] P. T. Brown, E. Guardado-Sanchez, B. M. Spar, E. W. Huang, T. P. Devereaux, and W. S. Bakr, Nat. Phys. **16**, 26 (2020).